Supplementary Information

Fluid flow and sperm guidance: a simulation study of hydrodynamic sperm rheotaxis

Kenta Ishimoto[1,2*] and Eamonn A. Gaffney[3†]

[1] The Hakubi Center for Advanced Research, Kyoto University, Kyoto, 606-8501, Japan
[2] Research Institute for Mathematical Sciences, Kyoto University, Kyoto, 606-8502, Japan
[3] Wolfson Centre for Mathematical Biology, Mathematical Institute, University of Oxford, Oxford OX2 6GG, UK

1 Parameter estimation

We detail the motivation for the parameter estimates used in Tables 1, 2 of the main text, which are recapitulated here for convenience in Supplementary Information Table 1.

The flagellar length L and the beat frequency T^{-1} are those of uncapacitated human sperm [8]. The predicted sperm trajectory is independent of the viscosity of the surrounding medium, μ, as the mass-scale does not enter the mapping between non-dimensional and dimensional trajectories and hence a viscosity estimate is not presented, though it must be such that the sperm flagellar waveforms used in this study are reasonable. The parameter α governs the flagellum wave chirality and a selection of values are considered, with $\alpha = 0$ constituting a planar waveform, $\alpha > 0$ a right handed helix as found in mouse [38] and $\alpha < 0$ gives a left handed helix, as observed for human sperm with $\alpha = -0.2$ [16, 17]. The parameter Γ controls the level of flagellar wave asymmetry, with infinite Γ corresponding to a symmetric flagellum whilst $\Gamma/L = 0.5$ gives circular swimming trajectories with a diameter of roughly the flagellum length, L, in Fig. 5 of the main text whilst sea urchin with asymmetric flagella waveforms have been observed to execute circles with diameters as small as 25 microns [37] or approximately 100 microns [23], depending on experimental details. The parameters k, B further describe the flagellar waveform, and the parameter estimates given are those of Dresdner and Katz [8], though in general these parameters are variable; finally the flagellar radius is based on images of the human sperm proximal flagellum, indicating a radius of approximately 500nm, though we do not consider the geometry of the tapering outer dense fibres found in mammalian sperm [11, 13].

*ishimoto@kurims.kyoto-u.ac.jp
†gaffney@maths.ox.ac.uk

Parameter	Interpretation	Value
L	Flagellar length	56μm
$1/T = \omega/[2\pi]$	Beat frequency	14 Hz
α	Chirality parameter	$\pm\{0, 0.01, 0.05, 0.1, 0.2\}$
Γ/L	Asymmetric waveform parameter	$\{0.5, \infty\}$
kL	Wavenumber	3π
B	Flagellar envelope parameter	$0.2L$
a	Flagellar radius	$0.01L$
$\dot{\gamma}$	Background shear flow strength	$0.1T^{-1}$
g/μ	Repulsion potential magnitude	$10LT^{-1}$
d	Repulsion potential lengthscale	$0.005L$

Table 1: Supplementary Information Table 1. Reference parameter values for the flagellum waveform, the shear flow strength and the repulsive surface potential.

To consider the shear flow strength, recall that $\boldsymbol{x} = (x_1, x_2, x_3) \equiv (x, y, z)$ are coordinates in the laboratory reference frame, and that the boundary where the repulsive surface potential is imposed corresponds to $z = 0$. Then, the extent of shear is given by $\dot{\gamma}$ and defined via the background flow velocity vector field, $\boldsymbol{u}^{\infty}(\boldsymbol{x}) = -\dot{\gamma} z \mathbf{e}_2$. The fact $\dot{\gamma}T$ is small indicates that we are considering a relatively weak shear flow relative to the velocity scales of sperm swimming at cell lengthscales away from $z = 0$, as generally required to prevent sperm washout from the system. The parameter g is the magnitude of the assumed repulsive surface forces at $z = 0$. Its scaling with viscosity, μ, is for convenience – we simply take g to be sufficiently high to ensure sperm do not crash into the boundary at $z = 0$; this is consistent with human sperm behaviour in glassware experiments once dilute human serum albumin is present in the media, which prevents sperm colliding with and sticking to the glassware [28].

Finally, the parameter $d = 0.005L = 280$nm is a measure of the repulsion potential decay length, which is larger than the measured scale of 50nm for bacteria [22], but the details close to the surface are qualitative only as the surface potential varies with the cell, solutes and surface and is not documented for sperm. The impact of variation in d on the quantitative details of trajectory curvatures is briefly presented in Fig 2d below, which shows that d influences trajectory curvatures, though not the qualitative details. Thus such uncertainty in the surface potential represents a source of modelling uncertainty which mitigates against the additional computational expense of including virtual sperm heads in the modelling. Further justification for this particular approximation follows in the next section.

2 Justifying the neglect of the sperm head

For sperm, the head is relatively small compared to the lengthscale of the flagellum and so we consider the errors associated with neglecting the head in calculating sperm trajectories, especially their curvature and thus the impact of rheotactic guidance cues.

For a small amplitude resistive force theory calculation, with a tangential resistance coefficient C_T, a spherical sperm head of lengthscale q and a flagellar wavenumber, k, head effects induce a correction

in the swimming speed at the order of [15]

$$\frac{6\pi q}{C_T L} = \frac{3q}{L}\left[\log\left(\frac{4\pi}{ak}\right) - \frac{1}{2}\right] \approx 8.1\frac{q}{L} \approx 0.2,$$

given the parameter values of Table 1 and $q \sim 1.6\mu$m, which is representative of human sperm.

We proceed to consider the scale of the head torque to the scale of the flagellum torque. Let $\boldsymbol{X}(s,t)$ denote the location of the flagellum at time t and arclength $s \in [0, L]$, and $\boldsymbol{F}$ denote the viscous drag per unit arclength at this location. Then the torque ratio is of the order of

$$\frac{8\pi\mu q^3\Omega}{|\int_0^L \boldsymbol{X} \wedge \boldsymbol{F}\mathrm{d}s|} \sim \frac{8\pi\mu q^3\Omega}{\frac{L}{2}C_T U L} \sim \frac{16\pi\mu q^3\Omega}{C_T U L^2} \sim \frac{8q^3\Omega}{UL^2}\left[\log\left(\frac{4\pi}{ak}\right) - \frac{1}{2}\right] \approx \frac{22q^3}{L^3}\frac{\Omega L}{U}.$$

For a trajectory with radius of curvature r_c, with T_c the time for a complete revolution if the angular velocity and translational velocities were fixed, one has $\Omega \sim 2\pi/T_c$ and $U \sim [2\pi r_c]/T_c$ so that $\Omega/U \sim 1/r_c$. For the tightest turning circle we consider in the results section of the main text $r_c \sim L/2$ whence the ratio of toque scales becomes

$$44\frac{q^3}{L^3} \approx 10^{-3}.$$

Hence the head torque scale is three orders of magnitude smaller than the flagellum torque scale, essentially as the ratio of head to flagellar torques scales with the cube of q/L rather than linearly, and thus head torques are subordinate and can be neglected.

Hence neglecting the sperm head entails that angular velocities are generally accurate and linear velocities are of the correct scale; further the linear velocity is always overestimated and hence the trajectory curvature underestimated. Thus neglecting the sperm head gives the correct scale of the rheotactic effect with a relatively small underestimation error motivating the neglect of the head, especially given quantitative accuracy is not feasible due to the modelling uncertainties associated with the parameter estimation of the repulsive surface potential.

3 The numerical algorithm and its validation

In this section, the numerical methods and algorithms are documented, together with modelling validation, including primary simulations for elliptical helicoidal beating sperm near a no-slip surface in the absence of background flow.

3.1 Numerical schemes

As spermatozoa are small enough to neglect inertia, the flow around the cell obeys Stokes' equations, which can be solved to within asymptotically small errors using the regularized Stokeslet method (RSM), as first developed by Cortez [6], though our implementation is analogous to that used in Gillies et al.'s computational study of human sperm [14].

The RSM method requires the regularized Stokeslet, which is a fundamental solution of Stokes' equations for an external force localised to within a lengthscale of ϵ of the point $\boldsymbol{x}_0$. There is not

a unique choice but a standard one is that the force at location $\boldsymbol{x}$ is given by $\boldsymbol{F}\psi_\epsilon(\boldsymbol{x},\boldsymbol{x}_0)$, with $\boldsymbol{F}$ constant, $\psi_\epsilon = 15\epsilon^4(r^2+\epsilon^2)^{-7/2}/8\pi$, $r = |\boldsymbol{x}-\boldsymbol{x}_0|$ and, with L denoting the flagellum length, ϵ is the regularisation lengthscale, with ϵ/L the parameter governing the asymptotic accuracy of the method.

In this instance, the regularized Stokeslet is given by

$$ {}^{\epsilon}G^S_{ij}(\boldsymbol{x}-\boldsymbol{x}_0;\epsilon) = \frac{(r^2+2\epsilon^2)\delta_{ij}+r_ir_j}{(r^2+\epsilon^2)^{3/2}}. \tag{3.1}$$

In presence of a rigid no-slip infinite plane wall, the regularized Stokeslet can be constructed by introducing additional localized functions [1], which reduce to the singular Blakelet solution [2] as $\epsilon \to 0$. We denote this regularised *Blakelet* by $\boldsymbol{G}^B$ and employ the representation in Smith [29], which modified the typographical sign error in Ainley et al. [1].

For a flat surface with no tangential stress, such as an air-water surface with high surface tension [19], another regularized Stokeslet can be constructed as in the singular Stokeslet case,

$$ {}^{\epsilon}G^I_{ij}(\boldsymbol{x},\boldsymbol{x}_0) = {}^{\epsilon}G^S_{ij}(\boldsymbol{x},\boldsymbol{x}^0) + (\delta_{ik}-2\delta_{i3}\delta_{k3}){}^{\epsilon}G^S_{kj}(\boldsymbol{x},\boldsymbol{x}^{0*}), \tag{3.2}$$

where $\boldsymbol{x}_0^*$ is the mirror image of $\boldsymbol{x}$ with respect to the boundary, given by $\boldsymbol{x}_0^* = \boldsymbol{x}_0 - 2(\boldsymbol{x}\cdot\boldsymbol{e}_z)\boldsymbol{e}_z$ with $\boldsymbol{e}_z$ the unit vector in the z-direction. Throughout this paper, we refer to this solution (3.2) as a regularized *Imagelet*, and utilise it when considering a virtual sperm near a flat surface at $z=0$ for a fixed tangential stress associated with a shear flow, so that the perturbation of the flow field due to the swimmer does not change the tangential stress at $z=0$.

While the boundary conditions associated with fixed tangential stress and a flat surface, that is zero normal velocity, at $z=0$ may not be relevant in most physical situations, and thus similarly for the Imagelet solutions, these solutions are nonetheless very informative in assessing the extent to which hydrodynamic interactions between the surface and the cell influence the rheotactic response. Analogous comments also hold for the Stokeslet solutions.

3.1.1 The boundary integral equation of the regularised Stokeslet method

Let $p^\infty(\boldsymbol{x})$, $\boldsymbol{u}^\infty(\boldsymbol{x})$ denote the pressure and velocity field of the background shear flow, which satisfy Stokes' equations and let p, $\boldsymbol{u}$ denote the flow field for the virtual sperm in this background flow. The linearity of Stokes equations ensures that $p-p^\infty$, $\boldsymbol{u}-\boldsymbol{u}^\infty$ also satisfy Stokes equations and thus the flow velocity field around a flagellum is asymptotically approximated by the regularised Stokeslet method [14] via the boundary integral equation

$$ u_i(\boldsymbol{x}_0) - u_i^\infty(\boldsymbol{x}_0) = -\frac{1}{8\pi\mu}\int_0^L \left[{}^{\epsilon}G^{(B,I,S)}_{ji}(\boldsymbol{X}(s,t),\boldsymbol{x}_0)f_j(\boldsymbol{X}(s,t))\right]\mathrm{d}s. \tag{3.3}$$

In the above, there is summation over repeated indices, μ is the fluid viscosity, $\boldsymbol{X}(s,t)$ is the laboratory frame location of the point an arclength s along the flagellum from its proximal end-point at $\boldsymbol{\xi}(s,t)=\boldsymbol{0}$ in the flagellar reference frame, at time t, and $\boldsymbol{f}(\boldsymbol{X}(s,t))$ is an unknown stress field defined on the flagellar centreline. The integral kernel ${}^{\epsilon}G^{(B,I,S)}_{ij}$ is the regularized version of the singular Blakelet, Imagelet or Stokeslet, according to the boundary conditions imposed at $z=0$. Note that with the regularised Blakelet, the no-slip boundary conditions at $x_3=0$ is automatically satisfied by $\boldsymbol{u}-\boldsymbol{u}^\infty$

and hence $\boldsymbol{u}$ up to $O(\epsilon)$, and analogously for the tangential stress and zero normal velocity boundary conditions associated with the Imagelet. The regularization parameter, ϵ, is chosen as $\epsilon = 0.32\Delta s$ with $\Delta s = L/N$ the discretisation length of the flagellum, where the number of discretisation points along the flagellum, N, is set to be $N = 60$. These particular choices are validated when the flagellum radius varies as a curved ellipsoid with minor axis equal to $0.01L$, as detailed in Gillies et al. [14].

The flagellar location in the laboratory frame, $\boldsymbol{X}(s,t)$ is related to its location with respect to the flagellar frame, $\boldsymbol{\xi}(s,t)$, by a translation and rotation: $\boldsymbol{X}(s,t) = \boldsymbol{X}(0,t) + \boldsymbol{R}\cdot\boldsymbol{\xi}(s,t)$. Hence, the no-slip condition at location $\hat{\boldsymbol{x}}_0$ on the boundary of the flagellum, approximated by enforcing it at the nearest point on the flagellar centreline $\boldsymbol{x}_0 \equiv \boldsymbol{X}(s_0,t)$, is given by the constraint that

$$\boldsymbol{u}(\boldsymbol{x}_0) = \boldsymbol{U} + \boldsymbol{\Omega}\wedge\boldsymbol{X}(s_0,t) + \boldsymbol{R}\cdot\dot{\boldsymbol{\xi}}(s_0,t),$$

where $\boldsymbol{U}$ and $\boldsymbol{\Omega}$ are respectively the linear and rotation velocity, given by $\dot{\boldsymbol{X}}(0,t) = \boldsymbol{U}$, and $\dot{\boldsymbol{R}} = \boldsymbol{\Omega}\wedge\boldsymbol{R}$.

Thus, $\boldsymbol{u}^{\infty}(\boldsymbol{x}_0)$ is the known background velocity flow field and one can write $\boldsymbol{u}(\boldsymbol{x}_0)$ in terms of the flagellar waveform, specified by the known function $\boldsymbol{\xi}(s,t)$, together with a linear combination of the components of the *a priori* unknowns, $\boldsymbol{U}$, and $\boldsymbol{\Omega}$. For a collocation of the flagellar centreline with N points we thus have $3N+6$ scalar unknowns: $\boldsymbol{U}$, $\boldsymbol{\Omega}$ and the stress field $\boldsymbol{f}$ at each collocation point. Enforcing equation (3.3) at each collocation point gives $3N$ scalar equations, whilst the final 6 scalar equations required for closure are given by the fact swimming occurs with no net force and torque, a further consequence of the negligible influence of inertia for cellular microswimmers.

Neutral buoyancy is implicitly assumed in these force and torque balances, as justified by the observations of Winet et al. [36] that boundary accumulation and rheotaxis completely dominate gravitational effects, and that sperm sedimentation speeds are 1-2 orders of magnitude slower than swimming speeds. Thus gravity is safely neglected. Taking into account the repulsive potential, the required six scalar force and torque balance equations for the sperm are explicitly given by

$$0 = \int_0^L [\boldsymbol{f} + \boldsymbol{f}^{rep}]\,\mathrm{d}s = \int_0^L \boldsymbol{X}\wedge[\boldsymbol{f} + \boldsymbol{f}^{rep}]\,\mathrm{d}s, \tag{3.4}$$

where $\boldsymbol{f}^{rep}$ is the force density due to the repulsive potential.

We refrain from using DVLO theory to determine this potential as this has been observed to be inaccurate with increasing osmolarity, even before physiological isotonicity is achieved [26], since the Debye layer shrinks to nanometer scales and other interactions dominate the surface interactions between the cell and a solid surface on the scale of tens to one hundred nanometres. Hence instead a simple repulsive potential, as also used by Spagnolie et al. [32], is implemented with

$$\boldsymbol{f}^{rep}(\boldsymbol{x}) = g\frac{e^{-z/d}}{1-e^{-z/d}}\boldsymbol{e}_z, \tag{3.5}$$

arising from non-hydrodynamical interactions, such as van der Waals forces, at $z = 0$. The parameters are presented in *Supplementary Information*, Table 1, and with this choice of $d = 0.005L$, sperm swimming is prohibited within a distance of approximately $0.01L = 2d$ from $z = 0$. As can be seen in Fig. 2(d)(e) changes in d do affect the surface induced-trajectory curvature as the cell boundary accumulation height changes, though we cannot distinguish a choice of d given the available data and, in any case, the surface repulsion potential is highly variable [22]. Nonetheless the qualitative conclusions are unaffected and thus so are the conclusions drawn in the main text.

Finally, the $3N+6$ scalar algebraic equations associated with a collocation point discretisation of (3.3) and (3.4) at a fixed point in time are subjected to singular preconditioning prior to solution via an LU factorisation. This yields the unknown surface stress $\boldsymbol{f}$ and, more importantly for our purposes, the linear and the angular velocities, $\boldsymbol{U}$ and $\boldsymbol{\Omega}$ at a fixed point in time. Thus the sperm position and orientation can be updated using these velocities. Iterating this process, which is performed via Heun's method [30, 20, 21], the sperm trajectory is generated, allowing the exploration of sperm boundary accumulation and rheotaxis.

3.2 Scheme validation

3.2.1 A comparison with other algorithms

For the validation of the RSM scheme above, we evaluated the swimming velocity during one beat cycle of a headless sperm flagellum in the absence of a surface repulsion potential or a boundary at $z = 0$. In addition we use the parameters

$$\alpha = 0,\ B = 1/2\pi,\ k = 2\pi,\ \omega = 1/2\pi,$$

with length and time in units of the flagellar length L and beat period T whilst the cell is initially located so that the body-fixed and the laboratory frame coincide. In Figure 1 these results for the RSM algorithm are compared with those obtained from Johnson's slender-body theory (SBT), as documented in Smith et al. [30], and direct numerical computation via the boundary element method (BEM), as detailed in Ishimoto & Gaffney [20, 21], analogously to the validation studies within Gillies et al. [14]. Figure 1 indicates the RSM scheme provides sufficient accuracy to analyse and discuss cell movement. More generally, mechanically based models have been shown to produce agreement with observation using flagellar waves extracted from video-microscopy, for instance [12, 14], emphasising that understanding sperm swimming can often be reasonably considered in terms of mechanics.

We also briefly note that it is inappropriate to quantitatively compare the regularised Stokeslet results here to the multi-particle collision results presented by Elgeti et al. [9, 10] and the slender body theory results of Smith et al., [30, 31] for the purposes of validation as the representation of surface forces differs across all three papers. In addition this entails that the results presented in this manuscript should not be used to distinguish between the discrepancy in the conclusions of Elgeti et al. [9] and Smith et al., [30], as documented in a correspondence [10, 31], whereby Elgeti et al. conclude that hydrodynamic flow fields induce sperm surface capture at much closer distances than Smith et al., who report boundary accumulation heights of very roughly 10 microns for a planar beater. Furthermore, we also note the results in the main text predict both larger mean boundary accumulation heights (main text, Fig 5b, red and orange curves, with mean boundary accumulation heights of about 8.5 microns) and also much closer surface swimming (Fig 5b, blue curve). Hence, even neglecting the absence of control for the surface forces, the results once more cannot be used to distinguish the discrepancy reported in the correspondence between Elgeti et al. and Smith et al. [9, 31].

3.2.2 A comparison with observations

We proceed to consider the behaviour of a virtual mouse sperm with no head and an elliptical helicoidal waveform near a no-slip surface at $x_3 \equiv z = 0$, in the absence of a background shear flow, with the

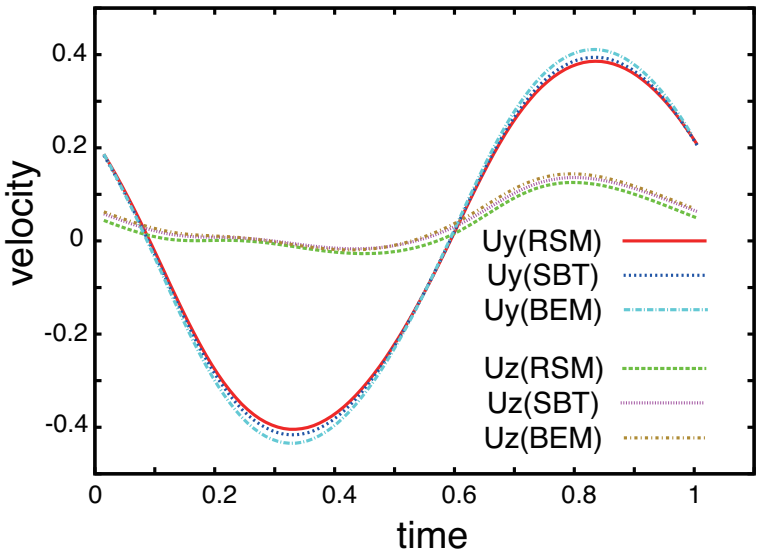

Figure 1: The linear velocity of the model spermatozoon during one beat cycle with three different numerical schemes: the regularized Stokeslet method (RSM), Johnson's slender-body theory (SBT), and direct numerical simulation via the boundary element method (BEM). Figure axes are non-dimensionalised using the flagellum length L as the lengthscale and the beat period T as the timescale.

parameters of Table 1, except that the flagellar length is $L = 120\mu$m, matching that of CD1 mice [34]. We further use a chirality parameter of $\alpha = 0.2$, matching the parity of mouse sperm chirality, and take $\Gamma = \infty$ so that the flagellar waveform is symmetric; the waveform is fully specified by equation (2.1) of the main text. A surface repulsion force, as given by equation (3.5) is also present in these simulations.

As generally the case with flagellar waveforms with non-trivial chirality, this virtual sperm is predicted to roll as it swims rather than asymptoting to a fixed orientation relative to the laboratory frame. Furthermore, boundary accumulation is predicted with the virtual sperm swimming adjacent to the no slip surface such that the axis of symmetry associated with the elliptical helicoidal waveform is rotated; hence the flagellar envelope is just offset from parallel to the no slip surface, as shown in Fig 2b. This gives a good qualitative comparison to Fig 2a, which is the sideview of flagellar beat patterns presented by Woolley as an illustration of the typical conical helicoid flagellar beat pattern exhibited by sperm near a no-slip surface [38]. Note however that these observations were made from above the cover slip but presented in a sideview, and thus assumed sufficient symmetry of the waveform, as is the case for a perfect conical helicoid. However, clearly Woolley's images suffer from making this approximation in that the flagellum penetrates the surface. In addition this alignment with a no-slip boundary for a sperm with an elliptical helicoid beat pattern is also seen in the slender body simulations of Smith et al. [30], though these latter simulations cannot be continued once the sperm approaches the surface, due to sperm crashing as no repulsion surface potential force is considered.

Woolley [38] also presented the projection of the trajectories of CD1 mouse sperm onto the no-slip surface, as reproduced in Fig 2c, with the analogous predictions for the virtual sperm presented in Fig 2d. Note that the direction of the predicted circling in Fig 2d agrees with observation, as does the presence of a lateral oscillatory displacement about the mean trajectory. Furthermore, the idealised

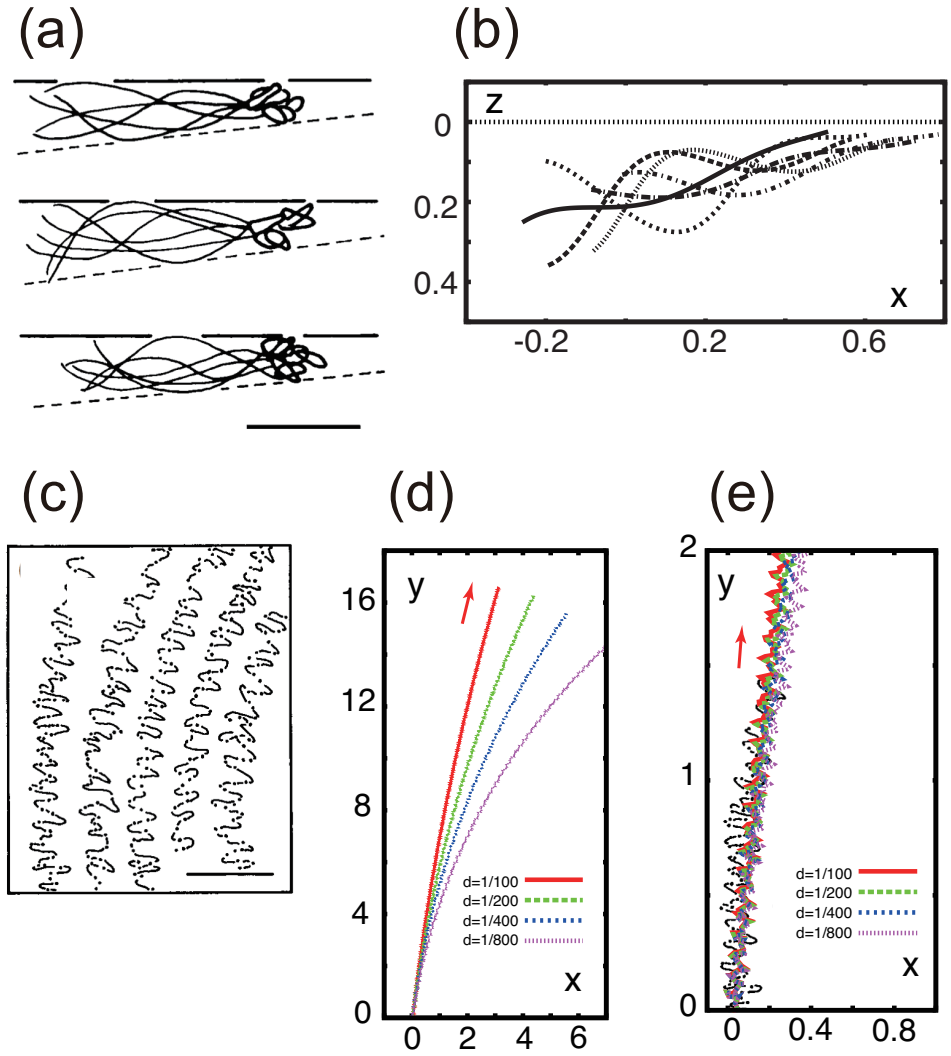

Figure 2: Sperm dynamics with elliptical helicoid beating, but no shear flow. (a) Observations of an elliptical helicoid beat at snapshots in time for individual Chinchilla sperm, scale bar 25μm [38]. (b) Snapshots of the elliptical helicoid beat, in sideview, for a virtual mouse sperm, which is predicted to swim adjacent to a no-slip boundary at $z = 0$; the simulations use the parameters given in Table 1 except that $L = 120\mu$m, the length of CD1 mice sperm observed by Vernon and Woolley [34]. In addition, the parameter choice of a symmetric flagellar wave with positive chirality was used, with $\Gamma = \infty$, $\alpha = 0.2$, $\boldsymbol{X}(s = 0, t = 0) = (0, 0, 0.1)$ and the initial inclination of the flagellum relative to the no slip plane at $z = 0$ was taken to be $\theta_{init} = 0.2\pi$. The snapshots for times t, given by $t/T \in \{10, 11, \ldots 15\}$, are superimposed, where T is the beat period. (c) The observed trajectories of CD1 mouse sperm, viewed from above, after accumulating at an upper coverslip [38]; scale bar 50μm. (d) The corresponding trajectory from computational simulations for the virtual CD1 mouse sperm used to generate plot (b), after projection onto the plane of the no-slip surface with an arrow depicting the direction of sperm swimming and the effect of varying d, in units of the flagellar length, L, depicted. (e) The trajectory of the lefthand trajectory of observed CD1 mice sperm in plot (c) is traced on the computed trajectory of virtual CD1 mice sperm for these different vales of d. Finally note that unit of length in plots (b), (d) is given by CD1 mouse flagellar length $L = 120\mu$m, and that (a), (c) have been reproduced from Woolley [38], with permission (Licence No. 3596460518634, Copyright © 2003, Society for Reproduction and Fertility).

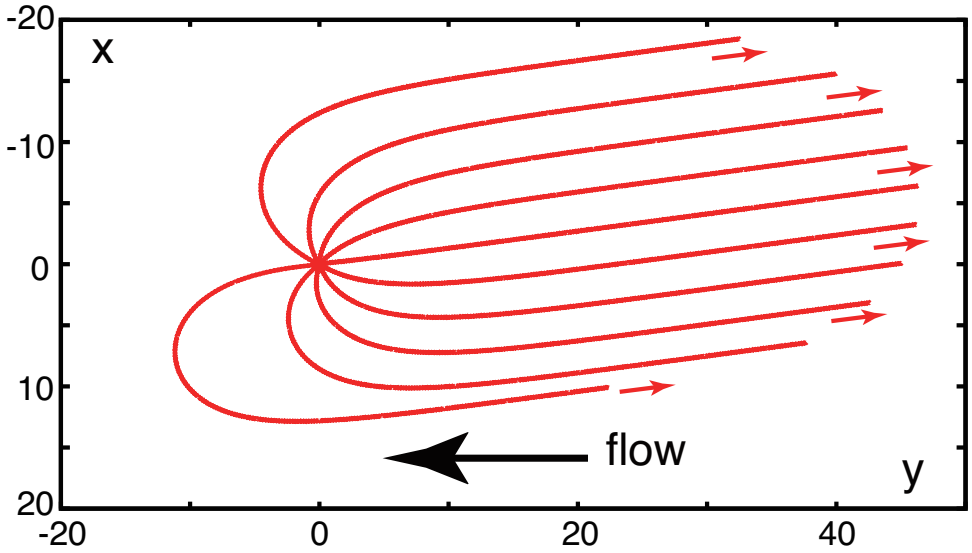

Figure 3: The effect of initial orientation on sperm trajectories for elliptical helicoid beating in a background flow, whose direction is depicted by the large arrow. The virtual sperm swimming trajectories are projected onto the x-y plane, with all axes in units of flagellum length, L. The simulations use the parameters presented in Table 1, with $\Gamma = \infty$ and $\alpha = 0.2$, and the cells are initially located at $\boldsymbol{X}(s = 0, t = 0) = (0, 0, 0.1L)$ with a trivial initial attack angle, $\theta_{init} = 0$, and thus are oriented parallel to the x-y plane. The initial orientation of the virtual sperm within the x-y plane however is taken from the values $\{0, 0.2\pi, \ldots, 1.8\pi\}$ and the resulting projections of the cell trajectories are plotted on the x-y plane, with small arrows depicting the direction of swimming.

waveform produces a trajectory that essentially agrees with observation, as shown in Fig 2e, where the leftmost trajectory of Fig 2c is superimposed with the trajectories of Fig 2d, after rescaling so that the lengthscales of each figure match. The only discrepancy is that the extent of the lateral displacement in the trajectory is slightly underestimated by the virtual sperm simulations, most likely due to our use of an idealised waveform; in particular note that prior studies demonstrating quantitative agreement featured the extraction of flagellar waveforms from video-microscopy. Nonetheless, here we observe predictions for the swimming sperm trajectory that qualitatively match observed trajectories for a number of CD1 mice sperm, overlapping with one from the cell sample in terms of the “value-averaged path” used in sperm diagnostics [35], which neglects lateral displacement as this does not contribute to sperm propagation on longer timescales.

4 The trajectories of sperm with different initial orientations

In the main text, the virtual sperm is initially oriented so that the ξ_3 axis coincides with x axis; this constraint is nonetheless without loss of generality. In Fig. 3, simulations for sperm with a symmetrical helical beat ($\Gamma = \infty, \alpha = 0.2$) and different initial orientations are shown. The virtual cells are always initially located at $\boldsymbol{X}(s = 0, t = 0) = (0, 0, 0.1L)$ with a no-slip boundary at $z = 0$, a background shear flow and trivial initial attack angle, $\theta_{init} = 0$, so that the cells are initially parallel to the x-y

plane. All further parameters are as in Table 1, though the initial direction of the sperm within the x-y plane is varied such that the angle made by the flow direction and initial sperm orientation takes the values $\{0, 0.2\pi, \ldots, 1.8\pi\}$. This includes an initial orientation directly into, and directly away from, the background flow. The resulting trajectories, as presented in Fig. 3, emphasise that the initial direction of the sperm does not affect the basic dynamics of sperm rheotaxis, as all trajectories ultimately exhibit the same asymptotic direction for the projection onto the x-y plane.

5 The trajectories of sperm with an asymmetric beat pattern and small chirality

Consider an asymmetric beat as illustrated in Fig. 1b of the main text. As observed in various marine species spermatozoa, such as sea urchin and *Ciona* [23, 27], an extensively asymmetric planar flagellar beat leads to a circling trajectory, in which the direction of the orbit is often selected so that all the cells rotate in the same direction. This selection is considered to be driven by a small chirality of the flagellar beat [18]. We explore the swimming trajectory of the asymmetric beating flagella in Fig. 4 using the parameters of Table 1, with $\Gamma = 0.5$, and a range of chiralities, $\alpha \in \{0, \pm 0.001, \pm 0.01\}$. The cell is initially located at $(0, 0, L)$ with the initial angle $\theta_{init} = 0$, so that it is oriented parallel to the laboratory x-y plane $z = 0$, which is a no-slip boundary in the simulations, and the surface repulsive potential force, equation (3.5), is also imposed.

The trajectory of the sperm with a planar beat ($\alpha = 0$, red curve) is a closed planar circle with transverse oscillations and a counterclockwise swimming direction when viewed above. With a slight chirality, the projected trajectory is not appreciably altered, though there is a slow drift in the z direction, which is reversed with a change in the sign of the chirality. With a further increase of the magnitude of chirality, the perpendicular drift is increased. Thus the counter-clockwise circling trajectory near a bottom boundary can only be found in a cell with a positive chirality, as negative chirality cells would not approach this boundary. If there was a no-slip boundary, for instance a coverslip, at $z =$ constant > 1, the negative chirality cell would approach the coverslip and thus exhibit a counter-clockwise rotation when viewed from above, corresponding to a clockwise trajectory viewed from the fluid, namely the opposite rotation direction to cells with positive chirality. Hence chirality is predicted to select the observed rotational direction for such swimmers. As a final remark, with a further increase in the magnitude of the chirality, the sperm trajectory becomes straighter, and thus tight circling in one direction near a boundary is only observed when the flagellar beat is both strongly asymmetric and nearly planar.

6 Estimates of rheotactic criteria

Sea Urchin Sperm Consider the sperm of the sea urchin Lytechinus, which have with $L \approx 45\mu$m, [4], a planar beat of frequency $\omega \approx 30$Hz and a swimming speed of 160μm [3]. Assuming a shear free turning circle of radius $R_{turn} \approx 25\mu$m, which is intermediate in the range reported by Woolley and Vernon [37] and Miki and Clapham [23], the above rheotactic condition for planar beaters, $\mathcal{R} := UR_{turn}/[L\omega H] \gg 4$ requires that the accumulation height satisfies $H \ll 750$nm. Furthermore the shear rate must be increased to beyond $\mathcal{S} := \dot{\gamma} R_{turn}/[\omega L] \gg 4$, and thus there is a lower bound of

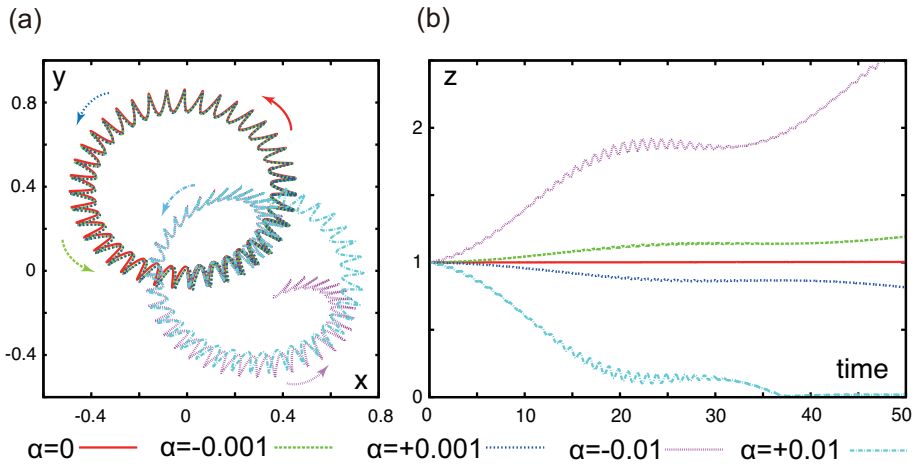

Figure 4: Sperm dynamics with an asymmetric beat pattern, but no shear flow. The simulations use the parameters given by Table 1, with $\Gamma = 0.5$ and α as depicted. The cells are initially located at $\boldsymbol{X}(s = 0, t = 0) = (0, 0, L)$ with the initial angle $\theta_{init} = 0$, and thus oriented parallel to the x-y plane. The no-slip boundary condition is imposed on $z = 0$, together with the repulsive surface potential force and all axes are in units of flagellum length, L, in the plots. (a) The projection of the sperm trajectories onto the x-y plane, which corresponds to trajectories viewed from above. All the cells reveal counter-clockwise rotation, reflecting the asymmetric beat. (b) Time evolution of z, the vertical distance above the no-slip boundary, for these cells.

the shear rate required for rheotaxis, $\dot{\gamma} \gg 140\text{s}^{-1}$. Firstly the accumulation height is much less than the lengthscale of the sea urchin sperm head, as deduced by inspection of the micrographs in [3]. Secondly, observed shear rates between murine ampulla mucosal folds are substantially less than 1s^{-1} by inspection of Fig 1d in [23] and thus these values of $\dot{\gamma}$ are orders of magnitude beyond the female reproductive tract flows that that have guided experimental scales. Consequently the absence of sea urchin rheotaxis in observational studies [23] is consistent with the modelling predictions.

CatSper-KO Sperm The CatSper-KO mouse spermatozoa examined in Miki & Clapham [23] were CatSper1 null and did not rheotax whilst presenting with circular rotation near a substrate. We assume mouse sperm parameters, $L \approx 80\mu$m [7], with a CatSper1 null mutant angular beat frequency of $\omega = 2\pi/T \approx 30$Hz, where T is the beat period, as reported by Carlson et. al. [5] in terms of the frequency $f = 1/T$ which was in the range [4Hz-8Hz]. From the observation of supplemental information videos presented by Miki and Clapham [23] we also have $U \approx 36\mu$m/s [23], and the shear-free turning circle radius is $R_{turn} \approx 40\mu$m. An estimation of the rheotactic criteria reveals that the accumulation height must satisfy $H \ll 150$nm and the shear rate must satisfy $\dot{\gamma} \gg 240\text{s}^{-1}$. Once more these constraints differ by orders of magnitude from the conditions in Miki and Clapham's experimental studies and thus the absence of rheotaxis is predicted, consistent with observation.

Hyperactivated Sperm Hyperactivated human sperm beat with a frequency of about $\omega \sim 15$Hz [24] whilst star-spin hyperactivated human sperm in media [25] exhibit tight circling on the scale of roughly 30 microns [33]; combined with the human flagellum length of 56μm rheotaxis requires shear rates on the scale $\dot{\gamma} \gg 30\text{s}^{-1}$ which is over a magnitude larger than the observed physiological and experimental scales. Hence rheotaxis is predicted to be absent under such conditions. In contrast, the

hyperactivation of mouse sperm in viscous solution, leads to much straighter swimming in Miki and Clapham's studies [23], indicating that rheotaxis would be predicted to occur, at least if boundary accumulation is present. However, the turning circle radius of these cells in the same study [23] is difficult to estimate given the limited length of the trajectories captured, and most likely highly variable preventing a more precise statement.

References

[1] J. Ainley, S. Durkin, R. Embid, P. Boindala, and R. Cortez. 2008, The method of images for regularised Stokeslets. *J. Comput. Phys.*, **227**, 4600–4616.

[2] J. R. Blake. 1971, A note on the image system for a stokeslet in a no slip boundary. *Proc. Camb. Phil. Soc.*, **70**, 303–310.

[3] C. J. Brokaw. 1965, Non-sinusoidal bending wave of sperm flagella. *J. Exp. Biol.* **43**, 155–169.

[4] C. J. Brokaw. 1991, Microtubule sliding in swimming sperm flagella - direct and indirect measurements on sea-urchin and tunicate spermatozoa. *J. Cell Biol.* **114**, 1201–1215.

[5] A. E. Carlson, R. E. Westenbroek, T. Quill, D. Ren, D. E. Clapham, B. Hille, D. L. Garbers, D. F. Babcock. 2003, CatSper1 required for evoked Ca^{2+} entry and control of flagellar function in sperm *Proc. Natl. Acad. Sci. U.S.A.*, **100**,14864–14868.

[6] R. Cortez. 2001, The method of regularized stokeslets. *SIAM J. Sci. Comput.* **23**, 1204–1225.

[7] J. M. Cummins and P. F. Woodall. 1985, On mammalian sperm dimensions. *J. Reprod. Fert.*, **75**,153–175.

[8] R. D. Dresdner and D. F. Katz. 1981, Relationships of mammalian sperm motility and morphology to hydrodynamic aspects of cell function. *Bio. Reprod.*, **25**, 920–930.

[9] Elgeti J, Kaupp UB, Gompper G. 2010, Hydrodynamics of sperm cells near surfaces. *Biophys. J.*, **99**, 1018–1026.

[10] Elgeti J, Kaupp UB, Gompper G. 2011, Response to comment on article: Hydrodynamics of sperm cells near surfaces. *Biophys. J.*, **100**, 2321–2324.

[11] D. W. Fawcett. 1975, The mammalian sperm. *Dev. Biol.*, **44**, 394–436.

[12] B. M. Friedrich, I. H. Riedel-Kruse, J. Howard, and F. Juelicher. 2010, High-precision tracking of sperm swimming fine structure provides strong test of resistive force theory. *J. Exp. Biol.*, **213**, 1226–1234, 2010.

[13] E. A. Gaffney, H. Gadêlha, D. J Smith, J. R. Blake, J. C Kirkman-Brown. 2011, Mammalian Sperm Motility: Observation and Theory, *Ann. Rev. Fluid Mech.*, **43**, 501-528.

[14] E. Gillies, R. M. Cannon, R. B. Green, and A. A. Pacey. 2009, Hydrodynamic propulsion of human sperm. *J. Fluid Mech.*, **625**, 445–474.

[15] J. Gray and G. J. Hancock. 1955, The propulsion of sea urchin spermatozoa. *J. Exp. Biol.*, **32**, 802–814.

[16] S. Ishijima, S. Oshio, and H. Mohri. 1986, Flagellar Movement Of Human-Spermatozoa. *Gamete Res.*, **13**, 185–197.

[17] S. Ishijima, M. S. Hamaguchi, M. Naruse, S. A. Ishijima, and Y. Hamaguchi. 1992, Rotational movement of a spermatozoon around its long axis. *J. Exp. Biol.*, **163**, 15–31.

[18] S. Ishijima, and Y. Hamaguchi. 1992, Relationship between direction of rolling and yawing of golden hamster and sea urchin spermatozoa. *Cell Struct. Funct.*, **17**, 319–323.

[19] K. Ishimoto and E. A. Gaffney. 2013 Squirmer dynamics near a boundary. *Phys. Rev. E*, **88**, 062702.

[20] K. Ishimoto and E.A. Gaffney. 2014, Swimming efficiency of spherical squirmers: Beyond the Lighthill theory. *Phys. Rev. E*, **90**, 012704.

[21] K. Ishimoto and E. A Gaffney. 2014, A study of spermatozoan swimming stability near a surface. *J. Theor. Biol.*, **360**, 187–199.

[22] J. D Klein, A. R. Clapp, and R. B. Dickinson. 2003, Direct measurement of interaction forces between a single bacterium and a flat plate. *J. Coll. Interface Sci.*, **261**, 379–385.

[23] K. Miki and D. E. Clapham. 2013, Rheotaxis Guides Mammalian Sperm. *Curr. Biol.*, **23**, 443–452.

[24] E. H. Ooi, D. .J Smith, H. Gadêlha, E. A. Gaffney, J. Kirkman-Brown. 2014, The mechanics of hyperactivation in adhered human sperm. *J. Roy. Soc. Open Science*, **1**, 140230.

[25] L. Robertson, D. P Wolf, and J. S Tash. 1988, Temporal Changes In Motility Parameters Related To Acrosomal Status - Identification And Characterization Of Populations Of Hyperactivated Human-Sperm. *Biol. Reprod.*, **39**, 797–805.

[26] Sharp JM, Dickinson RB. 2005, Direct evaluation of DLVO theory for predicting long-range forces between a yeast cell and a surface. *Langmuir*, **21**, 8198–8203.

[27] K. Shiba, S. A. Baba, T. Inoue, and M. Yoshida. 2008, Ca^{2+} bursts occur around a local minimal concentration of attractant and trigger sperm chemotactic response . *Proc. Natl. Acad. Sci. U.S.A.*, **105**, 19312–19317.

[28] D. J. Smith, E. A. Gaffney, H. Gadhêla, N. Kapur, and J. C. Kirkman-Brown. 2009, Bend propagation in the flagella of migrating human sperm, and its modulation by viscosity. *Cell Motil. Cytoskel.*, **66**, 220–236.

[29] D. J. Smith. 2009, A boundary element regularized Stokeslet method applied to cilia- and flagella-driven flow *Proc. Roy. Soc. A*, **465**, 3605–3626.

[30] D. J. Smith, E. A. Gaffney, J. R. Blake, and J. C. Kirkman-Brown. 2009, Human sperm accumulation near surfaces: a simulation study. *J. Fluid Mech.*, **621**, 289–320.

[31] Smith DJ, Gaffney EA, Shum H, Gadêelha H, Kirkman-Brown J. 2011, Comment on the article by J. Elgeti, U. B. Kaupp, and G. Gompper: Hydrodynamics of sperm cells near surfaces. *Biophys. J.*, **100**, 2318–2320.

[32] S. E Spagnolie and E. Lauga. 2012, Hydrodynamics of self-propulsion near a boundary: predictions and accuracy of far-field approximations. *J. Fluid Mech.*, **700**, 105–147.

[33] T. Su, L. Xue and A. Ozcan. 2012, High-throughput lensfree 3D tracking of human sperms reveals rare statistics of helical trajectories. *Proc. Natl. Acad. Sci. U.S.A.*, **109**, 16018–16022.

[34] G. G. Vernon and D. M. Woolley. 2002 Functional state of the axonemal dyneins during flagellar bend propagation. *Biophys. J.*, **83**, 2162–2169.

[35] WHO. 2010 *World Health Organization, Department of Reproductive Health and Research. WHO laboratory manual for the Examination and processing of human semen.* World Health Organization.

[36] H. Winet, G. S. Bernstein, and J. Head. 1984, Observations on the response of human spermatozoa to gravity, boundaries and fluid shear. *J. Reprod. Fert.*, **70**, 511–523.

[37] D. M. Woolley, G. G. Vernon. 2001, A study of helical and planar waves on sea urchin sperm flagella, with a theory of how they are generated. *J. Exp. Biol.* **204**, 1333–1345.

[38] D. M. Woolley. 2003, Motility of spermatozoa at surfaces. *Reproduction*, **126**, 259–270.